RSC Advances

PAPER

View Article Online
View Journal | View Issue



Cite this: *RSC Adv.*, 2026, **16**, 586

# Effect of temperature and gamma irradiation on dielectric properties of $FeGaInS_4$/PVA composites

Zeynab Addayeva, *[ab] Mustafa Muradov,[a] Goncha Eyvazova,[a] Namiq Niftiyev,[c] Yashar Azizian-Kalandaragh,[de] Faik Mammadov[cf] and Elchin Huseynov[g]

In this study, the effects of gamma radiation at various doses (500, 1500, and 2500 kGy) on nanocomposites synthesized by incorporating $FeGaInS_4$ layered semiconductor crystals into a PVA matrix at a concentration of 3 wt% were investigated. The aim of the research was to determine how radiation-induced structural and functional changes affect the dielectric and optical properties of the composite. The nanocomposites were synthesized using the solution casting method and analyzed before and after radiation using X-ray diffraction (XRD), UV-Vis spectroscopy, and dielectric spectroscopy techniques. XRD results indicated that at a lower radiation dose (500 kGy), cross-linking was predominant, leading to increased crystallinity. In contrast, at higher doses (1500 and 2500 kGy), chain scission became dominant, causing structural disorder and amorphization. UV-Vis analysis showed a decrease in absorption and an increase in transmittance. Moreover, the optical band gap ($E_g$) and Urbach energy ($E_u$) were found to be highly sensitive to the radiation dose. Dielectric measurements revealed that the highest values of the real part of permittivity ($\varepsilon'$) and dielectric loss tangent (tg $\delta$) were obtained at a radiation dose of 500 kGy, attributed to interfacial polarization and the formation of dipolar groups. The electrical conductivity followed the correlated barrier hopping (CBH) mechanism, with activation energy decreasing as the radiation dose increased. In conclusion, low-dose gamma radiation enhanced the structural stability and electro-optical performance of the nanocomposites, while higher doses led to degradation and a decline in functional properties. These findings underscore the practical significance of radiation-controlled material engineering.

Received 26th October 2025
Accepted 15th December 2025

DOI: 10.1039/d5ra08220j

rsc.li/rsc-advances



## 1 Introduction

Polymer-based materials have gained significant importance in recent decades as functional dielectrics with broad application potential in advanced technological fields.[1] Their mechanical, electrical, and thermal properties are closely related to their internal structural organization—particularly the degree of crystallinity *versus* amorphousness, molecular arrangement, and morphological characteristics.[2] To enhance the structural properties and expand the application areas of polymer systems such as polyethylene (PE), ethylene-vinyl acetate (EVA), and polyvinyl alcohol (PVA), the incorporation of nano- and micro-sized filler particles (*e.g.*, nanoclays, layered sulfides, carbon nanotubes) has been widely employed and is now considered a standard approach in modern materials engineering.[3]

The functional performance of polymer composites depends not only on the chemical nature and geometry of the fillers but also on the processing and modification techniques applied.[4] These modifications improve the operational stability of materials and broaden their application environments. One such effective technique is gamma irradiation, which can significantly alter the electrical conductivity, dielectric stability, surface, and volume resistivity of polymers.[5,6] The interaction of gamma photons with the polymer matrix leads to various physicochemical changes such as chain scission, oxidation, and crosslinking. The direction and dominance of these effects depend on factors such as irradiation dose, polymer type, and the surrounding environment (*e.g.*, presence of oxygen).[7–9]

High-energy γ-photons disrupt the electronic structure of the polymer chains and generate primary radical centers (R$^{\bullet}$). These radicals can either initiate chain scission processes (β-scission, H-abstraction) or form new covalent bonds through crosslinking. Crosslinking typically increases the molecular weight of the polymer and enhances its thermal and mechanical stability. However, in oxygen-rich environments and at high radiation doses, oxidative degradation processes dominate, resulting in the formation of carbonyl and carboxyl functional

[a]*Baku State University, Nano Research Laboratory, Baku, Azerbaijan. E-mail: zeynabaddayeva@gmail.com*
[b]*Baku State University, Faculty of Physics, Department of Physics of Semiconductor, Azerbaijan*
[c]*Azerbaijan State Pedagogical University, Baku, Azerbaijan*
[d]*Photonics Application and Research Center, Gazi University, 06500 Ankara, Turkey*
[e]*Photonics Department, Applied Science Faculty, Gazi University, 06500 Ankara, Turkey*
[f]*Institute of Catalysis and Inorganic Chemistry, Baku, Azerbaijan*
[g]*Institute of Radiation Problems of the Ministry of Science and Education of the Republic of Azerbaijan, B.Vahabzade 9, Baku, AZ 1143, Azerbaijan*

groups that impair the material's stability and dielectric properties.[8–11]

Thus, the overall effect of gamma irradiation on polymers is governed by the balance between chain scission and cross-linking. Optimizing this balance requires careful control over irradiation parameters. Moreover, the scale and nature of these changes also depend on the type and morphology of the fillers used in the polymer matrix.[12–19] For instance, previous studies have shown that the addition of one-dimensional (1D) or two-dimensional (2D) nanostructured fillers into PVA matrices leads to more distinct and selective radiation-induced transformations, as evidenced by the shift of crystallinity peaks and the appearance of new phases in XRD patterns.[14]

In the present study, polyvinyl alcohol (PVA) was selected as the matrix material. As a semi-crystalline polymer, PVA undergoes two primary processes under γ-irradiation: chain scission and inter-chain cross-linking. These radiation-induced effects can lead to significant changes in the polymer's morphological and physical properties.[10,14]

$FeGaInS_4$ layered crystal was chosen as the filler material in this work. $FeGaInS_4$ is a p-type, thermally sensitive semiconductor known for its promising structural and functional properties, making it a suitable candidate for various sensor and optoelectronic applications.[20–22] It has an energy band gap of approximately 1.46 eV, and its electrical conductivity increases with temperature-primarily attributed to a thermally activated hopping mechanism.[22,23] This mechanism, which facilitates electron transitions between localized states, exhibits an activation energy of around 0.21 eV.[24] Due to the presence of iron (Fe) ions, the material also displays magnetic characteristics.[25,26]

In this study, PVA/$FeGaInS_4$ polymer composites were synthesized using the solution casting method and exposed to gamma radiation at doses of 500 kGy, 1500 kGy, and 2500 kGy. The effects of gamma irradiation on the structural and dielectric properties of these composites were systematically investigated. Crosslinking is known to reduce the water solubility of PVA and improve its mechanical strength, elasticity, chemical resistance, and thermal stability, thereby expanding its applicability in fields such as radiation-resistant coatings, dielectric components, packaging materials, hydrogels, and flexible electronics. In the present study, different irradiation doses were employed to determine the dose window capable of inducing effective crosslinking in the PVA-based composite without triggering significant structural degradation. The choice of including high-dose irradiation regimes was motivated by previous studies on PVA/GO systems, where similarly high γ-irradiation doses did not produce detectable macroscopic degradation. Therefore, investigating a broad dose range allowed us to systematically evaluate dose-dependent structural, dielectric, and interfacial responses and to identify the threshold at which crosslinking remains beneficial while avoiding dose-induced deterioration of the polymer-filler interface[27–29]

# 2 Materials and methods

## 2.1 Synthesis of $FeGaInS_4$/PVA composites

$FeGaInS_4$/PVA nanocomposites were fabricated using a solution casting technique. Initially, $FeGaInS_4$ crystals were synthesized separately before being incorporated into a 5 wt% aqueous solution of polyvinyl alcohol (PVA).

The $FeGaInS_4$ crystals were synthesized by combining equimolar (1 : 1 molar ratio) amounts of $FeGa_2S_4$ and $FeIn_2S_4$, which were sealed in an evacuated quartz ampoule. The sealed ampoule was then thermally treated in a dual-zone furnace at 800 K for 100 hours to facilitate crystallization, following procedures reported in the literature.[20–23]

For composite preparation, a 5 wt% PVA solution was first prepared. Subsequently, $FeGaInS_4$ powder was added at a concentration of 3 wt% relative to the PVA content. The mixture was subjected to ultrasonication for 4 minutes to ensure uniform dispersion of the filler particles. The resulting solution was then cast into Petri dishes and allowed to dry at room temperature. Once completely dried, the flexible composite films were carefully peeled from the dishes and cut into appropriate dimensions for gamma irradiation.

Gamma irradiation was carried out at doses of 500, 1500, and 2500 kGy using a cobalt-60 ($^{60}Co$) gamma source. The average energy of the γ-radiation was approximately 1.25 MeV, with individual γ-quanta having energies up to 1.33 MeV.

## 2.2 Characterization of $FeGaInS_4$/PVA composites

The structural and dielectric properties of the prepared composite films were investigated using X-ray diffraction (XRD), UV-Vis spectroscopy, and dielectric spectroscopy.

XRD analyses were carried out using an APD 2000 PRO diffractometer equipped with Ni-filtered Cu-Kα radiation ($\lambda$ = 1.5406 Å) over a $2\theta$ range of 5–80°, enabling the identification of crystalline phases and the evaluation of structural modifications induced by gamma irradiation.

The optical properties of the composites were characterized using a Specord 250 Plus UV-Vis spectrophotometer in the wavelength range of 430–1100 nm. This analysis provided information on absorption behavior, transmittance, and changes in the optical band gap.

Dielectric measurements were conducted using an E7-20 dielectric spectrometer operating over a frequency range from $1.2 \times 10^2$ Hz to $10^6$ Hz and a temperature range of 293 K to 373 K. These measurements were used to determine permittivity ($\varepsilon'$), dielectric loss (tg $\delta$), and electrical conductivity parameters.

Together, these characterization techniques provided comprehensive insight into the effects of gamma irradiation on the structural, optical, and dielectric performance of the $FeGaInS_4$/PVA nanocomposites.

## 2.3 Calculation methods

**2.3.1 XRD analysis.** X-ray diffraction (XRD) spectra are widely used to determine crystallite size, structural defects, and internal stresses in materials. The crystallite size of a sample can be calculated using the Scherer equation,[30] which is expressed as:

$$D = \frac{k\lambda}{\beta \cos \theta} \quad (1)$$

where: $D$ represents the average size of ordered (crystalline) domains, which can be smaller than or equal to the grain size, and the grain size can be smaller than or equal to the particle size. $k$ is a dimensionless shape factor with a standard value of about 0.9, usually close to 1, depending on the shape of the crystallites. $\lambda$ is the wavelength of the X-rays. $\beta$ is the line broadening at half maximum intensity (FWHM) after calculating the instrumental broadening, expressed in radians. This value is sometimes called $\Delta(2\theta)$. $\theta$ is the Bragg angle in radians.

Additionally, the micro strain ($\varepsilon$), which quantifies the lattice distortions, can be estimated from the peak broadening using the following relation:

$$\varepsilon = \frac{\beta}{4\tan\theta} \tag{2}$$

where: $\beta$ is the FWHM of the peak in radians. $\theta$ is the Bragg angle in radians.

Although the Scherer equation is widely used, it has limitations due to its sensitivity to peak broadening contributions from factors other than crystallite size. Micro strain, which arises from lattice distortions due to defects, dislocations, or stresses, can significantly contribute to XRD peak broadening. Consequently, the Williamson–Hall (W–H) method is often preferred, as it offers a more comprehensive approach by simultaneously evaluating both crystallite size and micro strain 31.

The W–H method distinguishes the contributions of size-induced and strain-induced broadening through a linear plot of $\beta\cos\theta$ *versus* $4\sin\theta$. The slope of this plot yields the micro strain ($\varepsilon$), while the intercept provides the crystallite size ($D$). This dual analysis makes the W–H method especially suitable for materials where strain effects cannot be ignored, such as nanostructured materials or those with significant lattice defects.[30,31] Defect density calculated using eqn (3)

$$\delta = D^{-2} \tag{3}$$

**2.3.2 UV-vis spectroscopy.** Absorption spectrum analysis is a fundamental technique to explore the band structure of materials. When a photon with a defined energy is absorbed, an electron transitions from a lower to a higher energy state.[32]

The optical band gap $E_g$ is extracted by extending the linear sections of these graphs to intersect the photon energy axis, following the relation:

$$(\alpha h\nu)^n = B(h\nu - E_g) \tag{4}$$

Here, $h\nu$ represents the photon energy, $B$ is a material-dependent constant, $\alpha$ is the absorption coefficient, and the exponent $n$ indicates the transition type, with $n = 0.5$ for indirect and $n = 2$ for direct transitions.[32–36]

The absorption coefficient $\alpha$ is calculated from absorbance data using the Beer–Lambert law:[33–36]

$$\alpha = \frac{2.303 \times A}{L} \tag{5}$$

where $A$ is the measured absorbance and $L$ is the film thickness in centimeters. Absorbance is defined as:

$$A = \log\left(\frac{I_0}{I}\right) \tag{6}$$

with $I_0$ and $I$ being the intensities of incident and transmitted light, respectively.

The Urbach energy ($E_u$) is a key parameter that characterizes the localized energy states existing below the optical band gap ($E_g$) in amorphous or defect-rich semiconducting and dielectric materials. This energy arises due to structural disorder, phonon interactions, and defect-induced states, which collectively lead to the formation of an exponential absorption tail—commonly known as the Urbach tail—in the sub-bandgap region of the absorption spectrum.[36]

To calculate the band gap energy, a graph of $(\alpha h\nu)^n$ *versus* $h\nu$ is plotted using the calculated absorption coefficient $\alpha$ and photon energy $h\nu$. The linear portion of this plot is extrapolated, and the point where it intersects the abscissa ($x$-axis) gives the value of $E_g$, the optical band gap energy.[35,36]

In the Urbach region, the optical absorption coefficient ($\alpha$) exhibits an exponential dependence on the photon energy ($h\nu$), which can be described by the following equation:

$$\alpha(h\nu) = \alpha_0 \cdot \exp\left(\frac{h\nu}{E_u}\right) \tag{7}$$

To determine the $E_u$, the natural logarithm of the absorption coefficient $\ln(\alpha)$ is plotted against the photon energy ($h\nu$). The resulting linear region of the plot allows for the extraction of $E_u$ from the inverse slope of the fitted line.[36]

**2.3.3 Dielectric spectroscopy.** In polymer materials, two primary charge transport models are observed: quantum mechanical tunnelling (QMT) and correlated barrier hopping (CBH).[37]

According to the CBH (correlated barrier hopping) model, the electrons in the electric field:

$$W = W_M - \frac{ne^2}{\pi\varepsilon\varepsilon_0 r} \tag{8}$$

Here, is the maximum height of the potential barrier, $\varepsilon$ is the dielectric constant of the material, $\varepsilon_0$ is the vacuum permittivity, $r$ is the distance between the two states of the charge carriers, and $n$ is the number of electrons undergoing the hopping process (which can take values of 1 for polaron and 2 for bipolar processes).[37]

For the electrical conductivity in the CBH model, the formula is:

$$\sigma(\omega) = \frac{\pi^3 N^2 \varepsilon\varepsilon_0 \omega {R_\omega}^6}{24}. \tag{9}$$

where $N$ is the density of pairs of states through which the charge carriers hop.

The relationship between the hopping distance $R_\omega$ and the potential barrier $W_M$ is given by:

$$R_\omega = \frac{e^2}{\pi\varepsilon\varepsilon_0}\left[W_M - kT\ln\left(\frac{1}{\omega\tau_0}\right)\right]^{-1}. \tag{10}$$

where $\tau_0$ – is the characteristic relaxation time, which is the inverse of the phonon frequency $\nu_f$.

The expression for the exponent $s$ as a function of the potential barrier height $W_M$:

$$s = 1 - \frac{6kT}{[W_M - kT/(\omega\tau_0)]}. \quad (11)$$

Eqn (7) can be simplified to:

$$s = 1 - \frac{6kT}{W_M}. \quad (12)$$

The theoretical study of the temperature dependence of conductivity based on Debye analysis of frequency dependence was considered in, where the temperature dependence of conductivity was determined as:[37–40]

$$\sigma(T)_\omega \sim T^{-1}\exp\left(\frac{T}{T_0}\right) \quad (13)$$

where $T_0$ is the characteristic temperature. According to eqn (13), for temperatures $T > T_0$ the dependence of electrical conductivity on temperature should yield a straight line in the $\ln(\sigma \cdot T) \sim f(T)$ coordinates.[36]

In the studied temperature range, electrical conductivity follows an activation mechanism and is described by the following equation:

$$\sigma = \sigma_0 \exp(-\Delta E/kT). \quad (14)$$

where $\Delta E$ is the activation energy, and $k$ is the Boltzmann constant.

### 2.4 Nomenclature of samples

Throughout the manuscript, the composite samples are denoted as follows:

N0 – 3 wt% $FeGaInS_4$/PVA (unirradiated),
N1 – 3 wt% $FeGaInS_4$/PVA irradiated with 500 kGy,
N2 – 3 wt% $FeGaInS_4$/PVA irradiated with 1500 kGy,
N3 – 3 wt% $FeGaInS_4$/PVA irradiated with 2500 kGy.

## 3 Results and discussion

### 3.1 XRD analysis

XRD analysis was performed to investigate the structural changes in the samples exposed to different doses of gamma radiation. Fig. 1 presents the XRD patterns of: (a) the synthesized FeGaInS4 crystal, and (b) 3 wt% $FeGaInS_4$/PVA composites subjected to gamma irradiation at various doses.

Fig. 1A presents the XRD pattern of the synthesized $FeGaInS_4$ crystal, which shows excellent agreement with previously reported data in the literature.[20–23]

Fig. 1B displays the XRD patterns of the PVA-based composite films containing 3 wt% $FeGaInS_4$, both unirradiated and subjected to gamma irradiation at doses of 500, 1500, and 2500 kGy.

The diffraction patterns exhibit well-defined peaks at $2\theta$ values of 7.153°, 14.41°, 21.72°, 28.2°, 30.95°, 37°, 40.8°, 44.74°, 53.5°, 61.2°, and 78.6°, which correspond to the (001), (002), (003), (102), (005), (104), (006), (105), (007), (008), (109), and (0010) crystallographic planes of $FeGaInS_4$, respectively. These results confirm that the $FeGaInS_4$ phase retains its crystalline integrity within the polymer matrix, consistent with previous reports.[20]

The sharp and intense nature of the diffraction peaks indicates a high degree of crystallinity. Importantly, the incorporation of PVA does not induce any significant shifts in peak positions or notable changes in intensity, suggesting that the crystal structure of $FeGaInS_4$ remains stable and undisturbed within the composite. This confirms the absence of any phase transformation resulting from polymer integration.[41]

Additionally, all composite samples exhibit a broad diffraction peak centered at approximately $2\theta \approx 19.31°$, corresponding to the (101) plane of semi-crystalline PVA. This characteristic feature is consistent with earlier reports[41] and confirms the successful incorporation of PVA in the composite films.

Based on the XRD data, the average crystallite size and micro strain (lattice strain) and defect density of the composites were calculated using the Williamson–Hall method and showed at

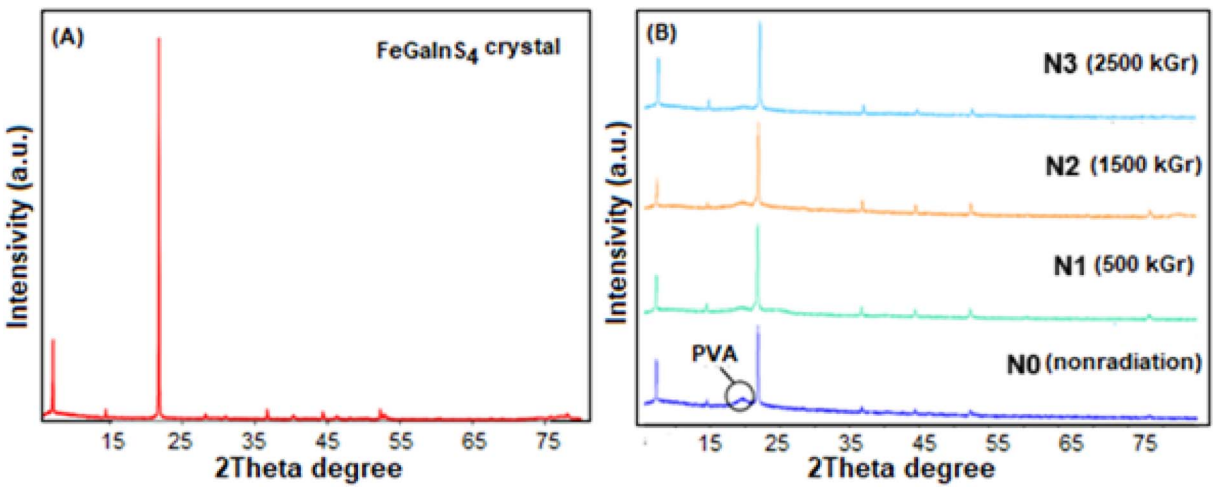


Fig. 1 XRD patterns of (A) the $FeGaInS_4$ crystal and (B) $FeGaInS_4$/PVA nanocomposites: (1) unirradiated-(N0), (2) 500 kGy-(N1), (3) 1500 kGy-(N2), (4) 2500 kGy-(N3).

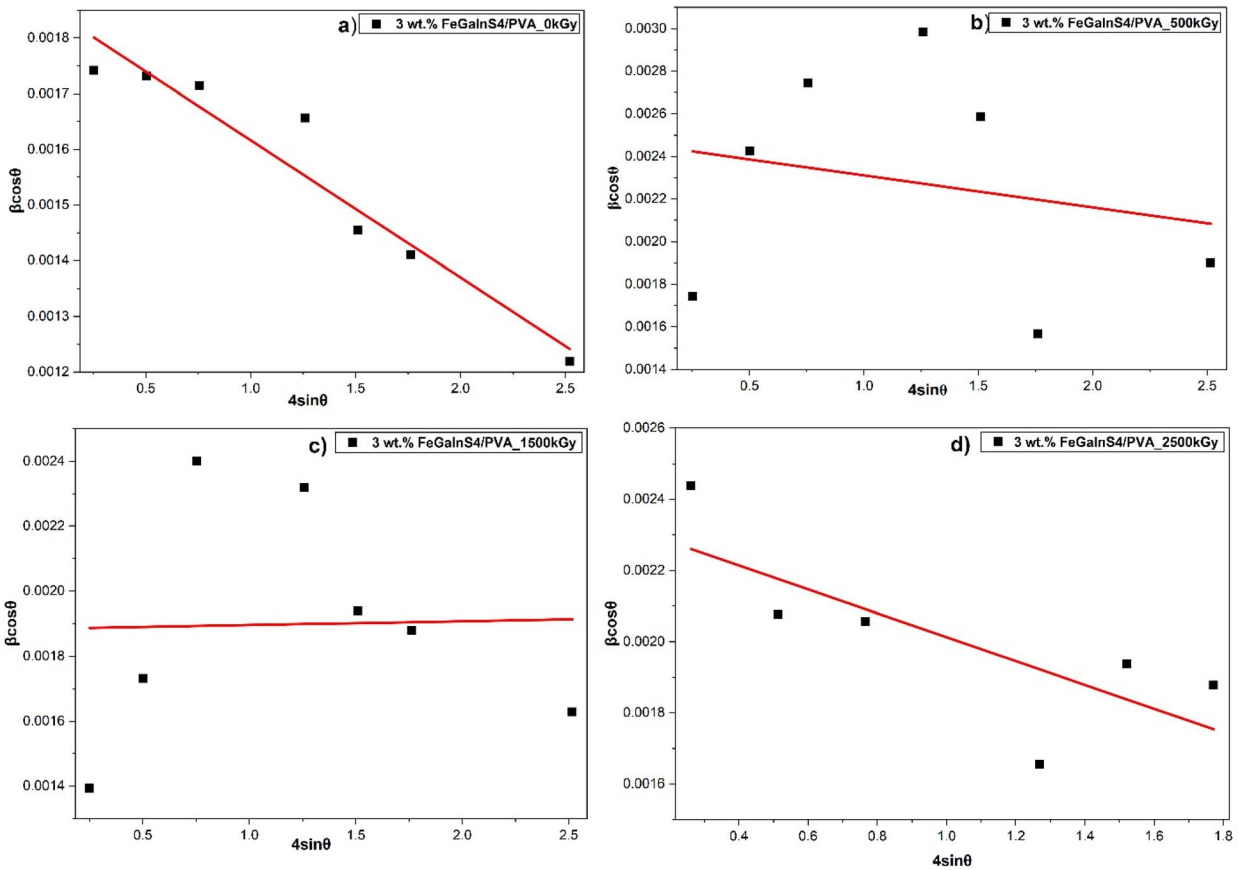


Fig. 2 Williamson–Hall plot of PVA based composites: (a) unirradiated-(N0), (b) 500 kGy-(N1), (c) 1500 kGy-(N2), (d) 2500 kGy-(N3).

Fig. 2 and data showed at Table 1. These values provide further insight into the effects of gamma irradiation on the crystalline structure and lattice dynamics of the nanocomposites.

The change of PVA's FWHM and defect density depending on radiation is shown in Fig. 3.

Gamma irradiation significantly affects the crystallinity, crystallite size, and internal strain (micro strain) of polymer-based composite materials. According to the results of Williamson–Hall analysis, the structural and parametric properties of PVA-based composites undergo systematic transformations under different radiation doses. These transformations are primarily attributed to two competing mechanisms: cross-linking and chain scission.

At a dose of 500 kGy, the composites exhibited a decrease in crystallite size and micro strain values, along with an increase in defect density. Moreover, a narrowing of the full width at half

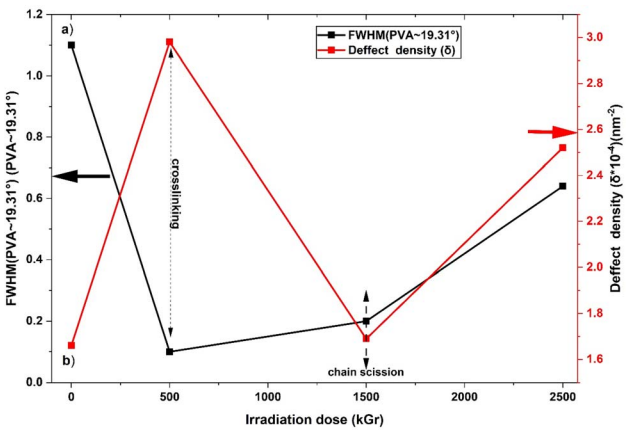


Fig. 3 Dependence of (a) PVA's FWHM and (b) defect density on irradiation.

Table 1 Structural parameters of polymer composites

| Sample | FWHM (PVA~19.31°) | Crystallite size (nm) | Micro strain $\varepsilon \times 10^{-6}$ | Deffect density $\delta \times 10^{-4}$ $(nm)^{-2}$ |
|---|---|---|---|---|
| N0 | 1.1 | 77.7 | −0.25 | 1.66 |
| N1 | 0.1 | 57.92 | −0.2 | 2.98 |
| N2 | 0.2 | 76.85 | 0.012 | 1.69 |
| N3 | 0.64 | 62.96 | −0.3 | 2.52 |

maximum (FWHM) at the characteristic PVA diffraction angle of 19.81° was recorded. These changes indicate that the crosslinking mechanism, which involves the formation of new chemical bonds between polymer chains under irradiation, dominates at this stage. As a result of crosslinking:

➢ Crystallites become more tightly packed within the matrix,
➢ Crystalline domains become more ordered,
➢ The degree of crystallinity in the PVA matrix increases.

The reduction in FWHM confirms enhanced crystallinity and structurally driven ordering promoted by irradiation.[42]

At 1500 kGy, an increase in both crystallite size and micro strain was observed, marking a transition from a compressive deformation regime to a tensile one. This suggests the onset of structural degradation within the PVA matrix. Radiation-induced chain scission in the polymer leads to:

➢ Partial detachment of crystallite particles from the matrix,
➢ Enlargement of these particles due to their release,
➢ Transformation of internal mechanical stresses into tensile-type microstrain.

These findings imply a shift from a crosslinking-dominant regime to a scission-dominant regime as the radiation dose increases.[43–45]

At the highest dose of 2500 kGy, a pronounced reduction in crystallite size and a significant increase in defect density were observed. The microstrain reached its maximum value among all samples, and the FWHM of the PVA peak at 19.81° was notably broadened. The broadening of FWHM and the reduction in crystallite size confirm that chain scission becomes dominant, leading to a substantial increase in the amorphous phase. At this stage, radiation effects are no longer limited to PVA chains alone; structural damage and defect formation are also evident in the filler particles.[42–46] Consequently:

➢ Degradation occurs in both the polymer matrix and the filler phase,
➢ Crystalline regions undergo fragmentation and deformation,
➢ Overall structural disorder and amorphous content are significantly increased.

### 3.2 UV-vis spectroscopy analysis

Absorption spectrum analysis is a fundamental technique used to investigate the electronic band structure of materials. When a photon with a specific energy is absorbed, an electron is excited from a lower to a higher energy state. By analyzing changes in the transmitted light intensity, one can deduce the nature of electronic transitions in the material.

Fig. 4 presents the UV-Vis spectra of 3 wt% $FeGaInS_4$/PVA composites under varying gamma irradiation doses. Specifically, samples N0 (unirradiated), N1 (500 kGy), N2 (1500 kGy), and N3 (2500 kGy) were studied.

Fig. 4a shows the absorbance spectra, while Fig. 4b correspondsto the transmittance spectra of the N0–N3 samples.

As seen from the absorbance spectra (Fig. 4a), the light absorption capability of the composite samples decreases with increasing radiation dose. At low radiation doses, cross-linking reactions dominate within the polymer matrix. The formation of chemical bridges between polymer chains leads to the deactivation of certain radiation-generated defect centers and results in a slight increase in structural order. The reduced defect density consequently causes a modest decrease in absorption.[46,47]

When the dose reaches 1500 kGy, chain-scission processes begin to occur, leading to the elimination of some absorption centers. At the same time, the radiation energy disrupts aggregated filler clusters, producing a more homogeneous dispersion of filler particles throughout the matrix. This homogenization significantly decreases light scattering and, therefore, enhances optical transmission. Additionally, surface trap states formed at this dose contribute to improved charge-transport behavior.

At the highest dose of 2500 kGy, chain scission becomes more intense. The functional groups and defect sites responsible for absorption—both within the polymer matrix and on the filler surfaces—are strongly reduced. As a result, absorption reaches its minimum and the material exhibits maximum transparency. Although XRD analysis indicates that long-range crystallinity remains largely preserved, an increase in short-

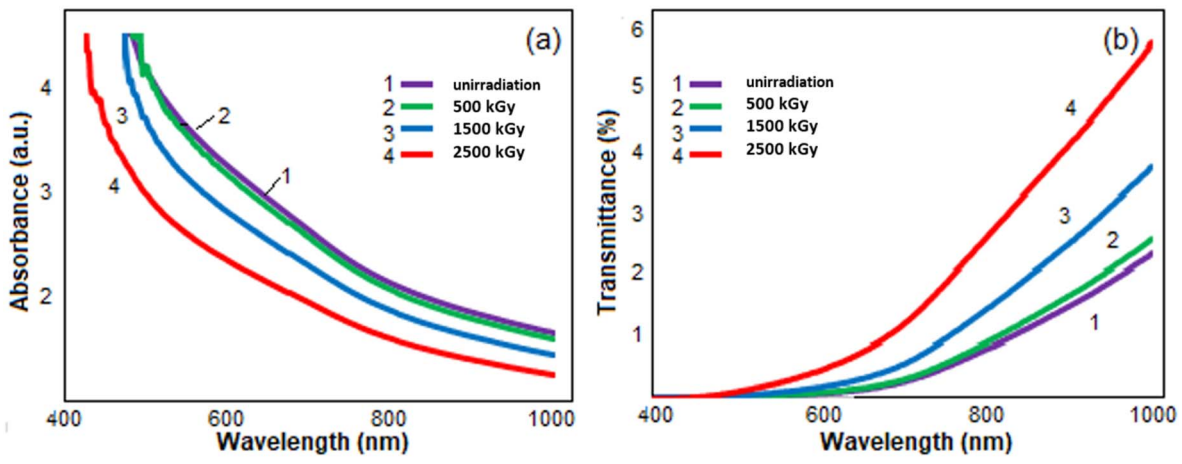


Fig. 4 UV-Vis spectra of $FeGaInS_4$/PVA nanocomposites at different γ-irradiation doses: (a) absorbance and (b) transmittance spectra for (1) N0 –(unirradiated), (2) N1 – (500 kGy), (3) N2 – (1500 kGy), (4) N3 – (2500 kGy).

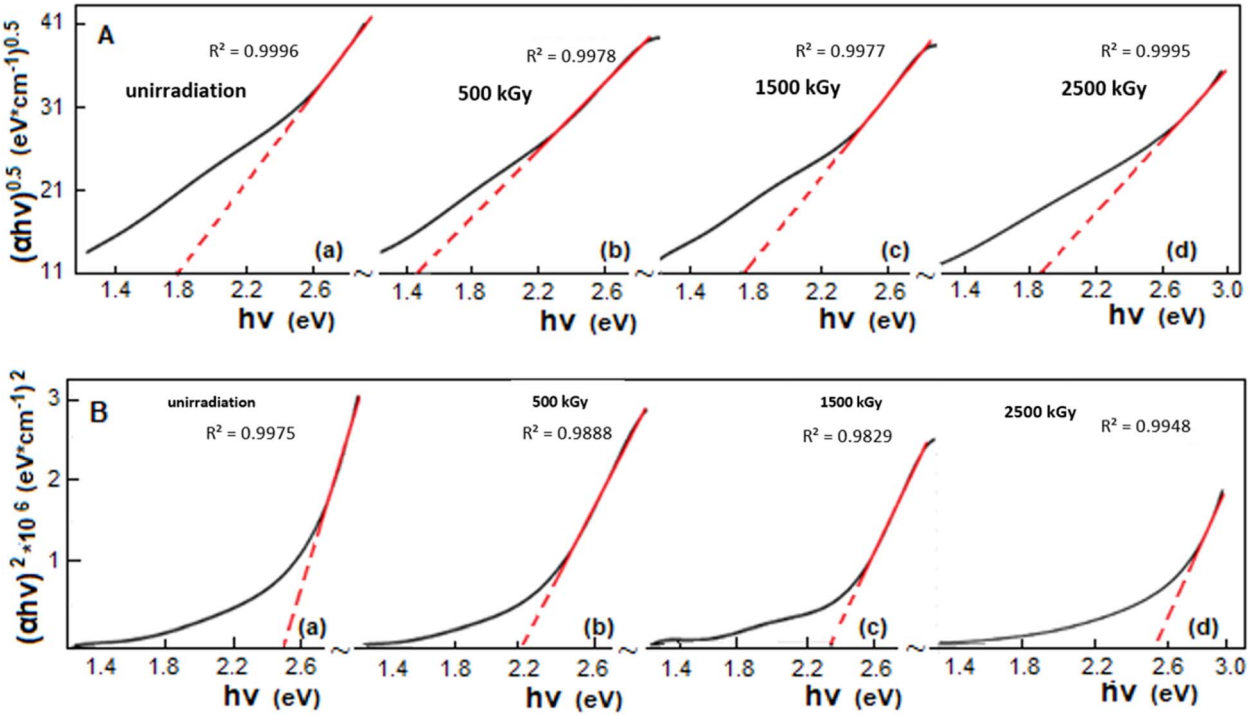


Fig. 5 (A) $(\alpha h\nu)^{0.5} \sim h\nu$ and (B) $(\alpha h\nu)^2 \sim h\nu$ for (a) unirradiated-(N0), (b) 500 kGy-(N1), (c) 1500 kGy-(N2), (d) 2500 kGy-(N3).

range chemical defects confirms that the reduction in absorption arises mainly from the deactivation of intrinsic absorption centers.[47]

According to studies reported in the literature,[32–36] near the fundamental absorption edge, both direct and indirect electronic transitions occur. These transitions are typically analyzed by plotting $(\alpha h\nu)^{0.5}$ and $(\alpha h\nu)^2$ *versus* the photon energy ($h\nu$). In this work, such plots are presented in Fig. 5(A) and (B for the nonirradiated and irradiated samples, respectively.

As shown in Fig. 5, for both transition types, the optical band gap ($E_g$) exhibits a characteristic non-monotonic evolution with increasing radiation dose. In the unirradiated sample, $E_g$ displays its initial value determined by the intrinsic polymer–filler electronic structure. Upon exposure to 500 kGy, the band gap decreases noticeably. At this stage, cross-linking is the dominant radiation process, which brings localized trap states closer to one another through the formation of inter-chain bridges. The reduced spatial separation and enhanced overlap of these states effectively narrow the band tail width, resulting in the minimum $E_g$ observed in Fig. 5A(b) and B(b).

At 1500 kGy, $E_g$ begins to increase again, as reflected by the shifted Tauc extrapolations in Fig. 5A(c) and B(c). This behavior is associated with the onset of chain-scission processes, which break polymer chains and increase the spacing between defect sites. As the localized states become more isolated, their electronic coupling weakens, leading to a moderate widening of the optical band gap. Although Eg increases relative to 500 kGy, it remains slightly lower than the pristine value due to the coexistence of both shallow radiation-induced states and improved filler dispersion.[48]

At the highest dose of 2500 kGy, the Tauc plots (Fig. 5A(d) and B(d)) reveal a pronounced increase in $E_g$. At this stage, intense chain scission generates a significant number of new defect centers, including deep-level states that introduce strong energetic disorder into the system. The formation of these deep defects widens the forbidden band gap and suppresses electronic transition probabilities, which is consistent with the large $E_g$ values extracted at this dose.[49]

Overall, the Tauc analysis confirms that the interplay between cross-linking (dominant at 500 kGy) and chain scission (dominant at ≥1500 kGy), together with the evolution of trap state distributions, governs the non-linear optical band gap behavior of the irradiated composites.

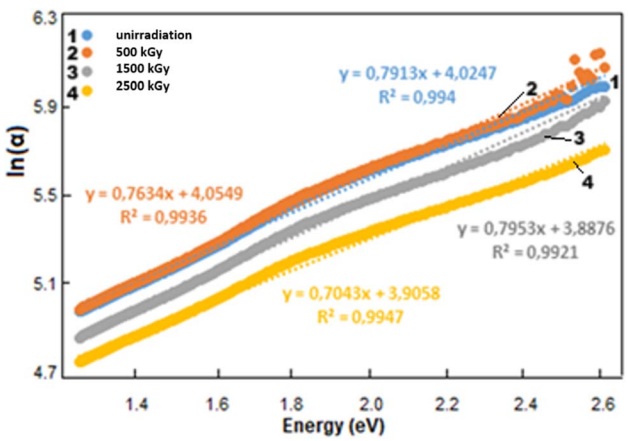


Fig. 6 The ln(α) *vs.* $h\nu$ dependence for (1) unirradiated-(N0), (2) 500 kGy-(N1), (3) 1500 kGy-(N2), (4) 2500 kGy-(N3).

The observed trend in $E_g$ is consistent for both indirect and direct band gap determinations. However, the fitting coefficient ($R^2$) of the Tauc plots is higher for the direct transition ($n = 0.5$) than for the indirect transition ($n = 2$), indicating that the material exhibits a dominant direct band gap behavior. Correspondingly, the absorption edge exhibits a similar trend with gamma irradiation. At 500 kGy, a slight red shift is observed, consistent with the decrease in $E_g$. As the irradiation dose increases to 1500 kGy, the edge shifts slightly back toward higher energies (blue shift), reflecting the partial recovery of $E_g$. At the highest dose of 2500 kGy, a more pronounced blue shift occurs, in line with the significant widening of the band gap. These shifts confirm that the spectral changes in the absorption edge follow the same tendency as the $E_g$ variations observed from the Tauc plots.

Based on the UV-Vis absorption spectra, the Urbach energy ($E_U$) was determined. This parameter provides important insights into the presence of localized defects, the degree of crystallinity, and structural order within the material. Fig. 6 shows the plots of ln($\alpha$) *versus* photon energy ($h\nu$) for the PVA+3 wt% $FeGaInS_4$ composites exposed to different radiation doses.

As shown in the figure, the unirradiated sample exhibited an Urbach energy ($E_u$) of 1.31 eV, indicating the presence of inherent disorder and initial defects within the material. Upon exposure to a 500 kGy radiation dose, $E_u$ decreased to 1.26 eV, which can be attributed to partial structural ordering and increased crystallinity at lower radiation doses. With further increase in radiation dose to 1500 kGy, Urbach energy reached a minimum value of 1.25 eV. This suggests that annealing effects due to irradiation reduced defects and led to relative structural stabilization. However, at higher doses (2500 kGy), a sharp increase in $E_u$ to 1.42 eV was observed, indicative of deep defect states and structural degradation induced by radiation. Such conditions generate broad energy tails for localized electron transitions, resulting in an exponential increase in the absorption edge region.[46–51]

The dependence of $E_g$ and $E_u$ on radiation dose is illustrated in Fig. 7.

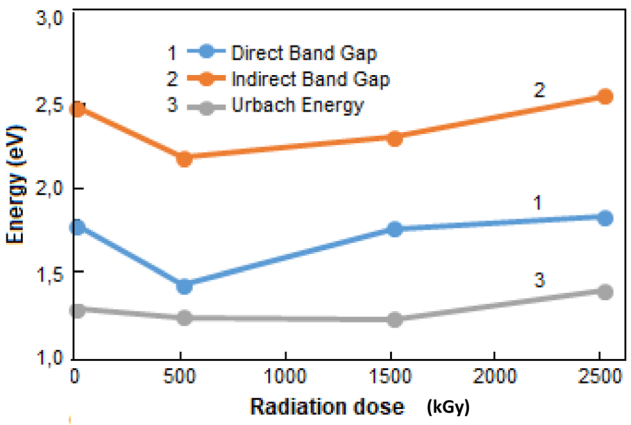


Fig. 7 Variation of $E_g$ and $E_u$ values as a function of radiation dose.

Table 2 Band gap energies ($E_g$) and Urbach energies ($E_u$) for polymer composites

| Sample | Direct band gap (eV) | Indirect band gap (eV) | Urbach energy (eV) |
|---|---|---|---|
| N0 | 1.8 | 2.49 | 1.31 |
| N1 | 1.45 | 2.2 | 1.26 |
| N2 | 1.78 | 2.32 | 1.25 |
| N3 | 1.85 | 2.56 | 1.42 |

The calculated band gap energies ($E_g$) and Urbach energies ($E_u$) for the studied films are summarized in Table 2.

### 3.3 Dielectric analysis

To evaluate the impact of gamma irradiation dose on the dielectric properties of polymer composites, the dielectric behavior of PVA+3 wt% $FeGaInS_4$ composites was studied over a temperature range of 293–373 K and an applied electric field frequency range from 120 Hz to 1 MHz. Fig. 8 illustrates the frequency dependence of the real part of the dielectric permittivity ($\varepsilon'$) at various temperatures for the following samples: N0 (unirradiated), N1 (500 kGy), N2(1500 kGy), and N3 (2500 kGy).

As observed in all the presented plots, the dielectric constant ($\varepsilon'$) decreases with increasing frequency across all radiation doses. At low frequencies, Maxwell–Wagner interfacial polarization dominates due to space charge accumulation at phase boundaries. However, at higher frequencies, dipolar polarization becomes the prevailing mechanism, and since molecular dipoles cannot reorient quickly enough in response to the rapidly oscillating field, $\varepsilon'$ decreases accordingly.[52–55]

Moreover, for all samples, the dielectric constant generally increases with temperature. This is attributed to the enhanced molecular mobility and likely increased interfacial polarization at elevated temperatures. Rising temperatures may also lead to partial plasticization of the polymer chains, facilitating the infiltration of PVA molecules between the $FeGaInS_4$ crystalline layers, which can expand the interfacial area and strengthen interphase polarization.[53,54]

Fig. 8a and b show that, compared to the unirradiated sample, $\varepsilon'$ appears to increase after 500 kGy irradiation. This effect is consistent with the interaction of high-energy γ-photons with the polymer matrix, which may break covalent bonds in the polymer chains and generate radicals. Some of these radicals could further fragment the polymer chains, while others might recombine to form crosslinked structures, increasing the compactness of the polymer network. Additionally, free polymer chains may react with environmental oxygen, forming oxygen-containing functional groups such as –OH, –C=O, –COOH, and –C–O–C, which are known to enhance dipolar polarization.[7–11] These mechanisms are therefore consistent with the observed increase in $\varepsilon'$, particularly in the frequency range of 1–100 kHz.

At 1500 kGy, polarization further appears to increase, potentially due to both chain scission and improved interaction between the polymer and $FeGaInS_4$ layers, as polymer chains may more effectively infiltrate the crystal structure. However, as

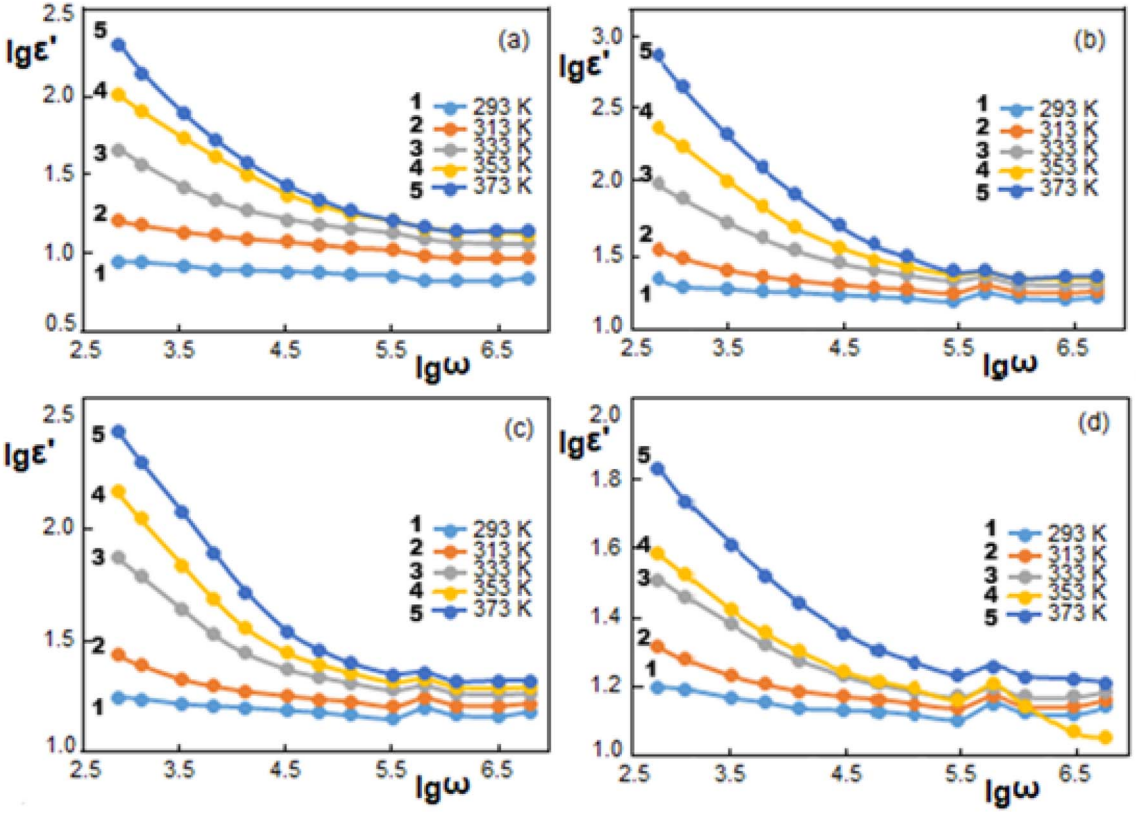


Fig. 8 Frequency dependence of the real part of dielectric permittivity ($\varepsilon'$) in the temperature range of 293–373 K for PVA+3 wt% $FeGaInS_4$ composites: (a) unirradiated-(N0), (b) 500 kGy-(N1), (c) 1500 kGy-(N2), (d) 2500 kGy-(N3).

seen in Fig. 8c, $\varepsilon'$ slightly decreases compared to the 500 kGy sample. This reduction could be related to the transformation of oxygen-based groups into less mobile secondary products at higher radiation doses, leading to a stiffer polymer network.[8–10]

At higher doses, the polarization trend reverses. Although a minor decrease in $\varepsilon'$ is observed at low temperatures (*e.g.*, 293–313 K), a more significant drop occurs at elevated temperatures. Notably, under these conditions, $\varepsilon'$ falls below that of the unirradiated sample. This behavior may result from the combined effects of high-dose irradiation and temperature-induced degradation. Defects forming in the interphase region and the potential instability of polar functional groups likely contribute to the observed reduction in dielectric permittivity. At a radiation dose of 2500 kGy, defects may develop not only in the polymer matrix but also around the $FeGaInS_4$ crystals, weakening the filler–polymer interaction. This effect is more pronounced at lower frequencies, highlighting the sensitivity of interfacial polarization to high radiation doses.[55–58] Fig. 9 illustrates the frequency dependence of the dielectric loss tangent (tan $\delta$) for the PVA/3 wt% $FeGaInS_4$ composite at various temperatures and gamma irradiation doses.

As seen in Fig. 9, at room temperature, the sample exposed to a 500 kGy gamma radiation dose exhibits the highest value of dielectric loss tangent (tg $\delta$). With further increases in the radiation dose, the tg $\delta$ value decreases. The physical processes occurring at lower radiation doses are primarily based on the breaking of covalent bonds and the subsequent formation of new covalent linkages through free radicals. Moreover, since irradiation was conducted in an oxygen-containing environment, additional polar functional groups are formed. These newly formed polar groups respond efficiently to the applied electric field, enhancing both the polarizability of the sample and the energy dissipated during polarization, thus increasing tg $\delta$.[54–57]

As the temperature increases (particularly at 333 and 353 K, the sample irradiated at 500 kGy still maintains the highest tg $\delta$ value, while samples exposed to higher radiation doses exhibit lower tg $\delta$ values compared to the unirradiated sample. As the temperature approaches the glass transition temperature ($T_g$), softening of the polymer matrix begins. Due to the presence of crosslinked structures and newly formed functional groups at the 500 kGy dose, the temperature response of the material shifts toward higher temperatures, allowing the sample to maintain its polarizability. However, at higher radiation doses, structural degradation of the polymer reduces its thermal stability, leading to softening at lower temperatures, which in turn diminishes polarization and the associated energy dissipation.[55–61]

At 373 K, the reduction in tg $\delta$ for the 500 kGy-irradiated sample compared to the pristine composite is attributed to the increased thermal stability provided by the crosslinked

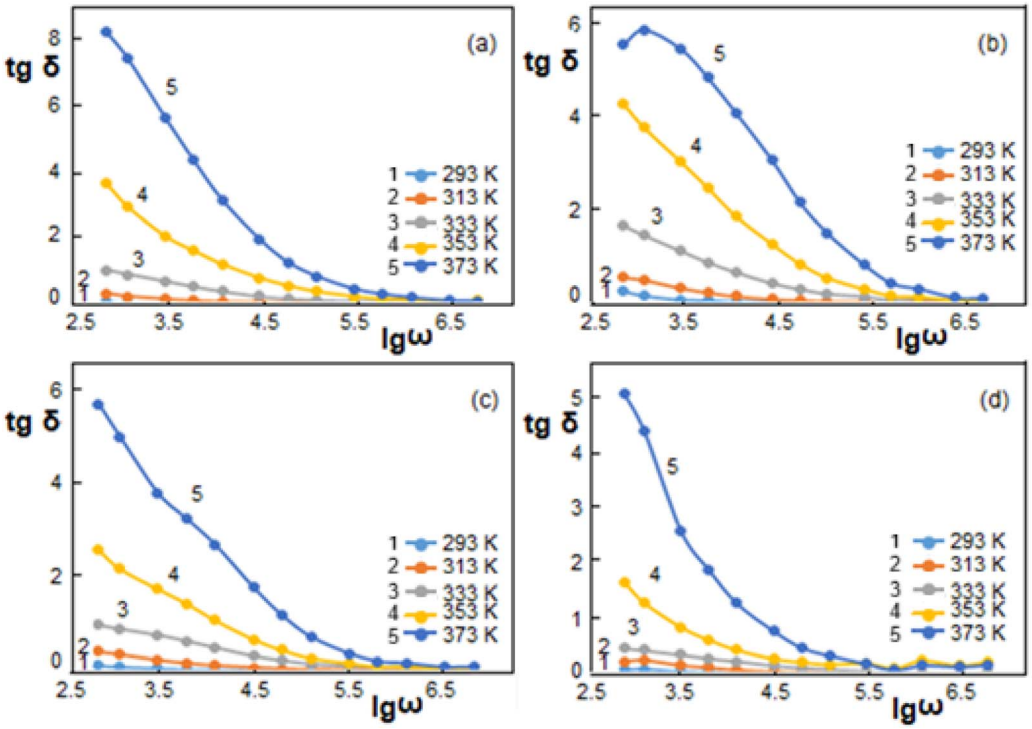


Fig. 9 Dependence of tg $\delta$ on the frequency of the electric field at temperatures ranging from 293 K to 373 K for the composites (a) unirradiated-(N0), (b) 500 kGy-(N1), (c) 1500 kGy-(N2), (d) 2500 kGy-(N3).

bonds and functional groups formed at this radiation dose. These structural features enable the composite to retain stability above $T_g$, resulting in lower energy dissipation during dipolar reorientation compared to the unirradiated sample.[52–57]

Furthermore, Fig. 9 reveals a shift of the tg $\delta$ peak toward higher frequencies specifically in the 500 kGy-irradiated sample. This peak corresponds to the material's relaxation time and typically occurs near the glass transition temperature.

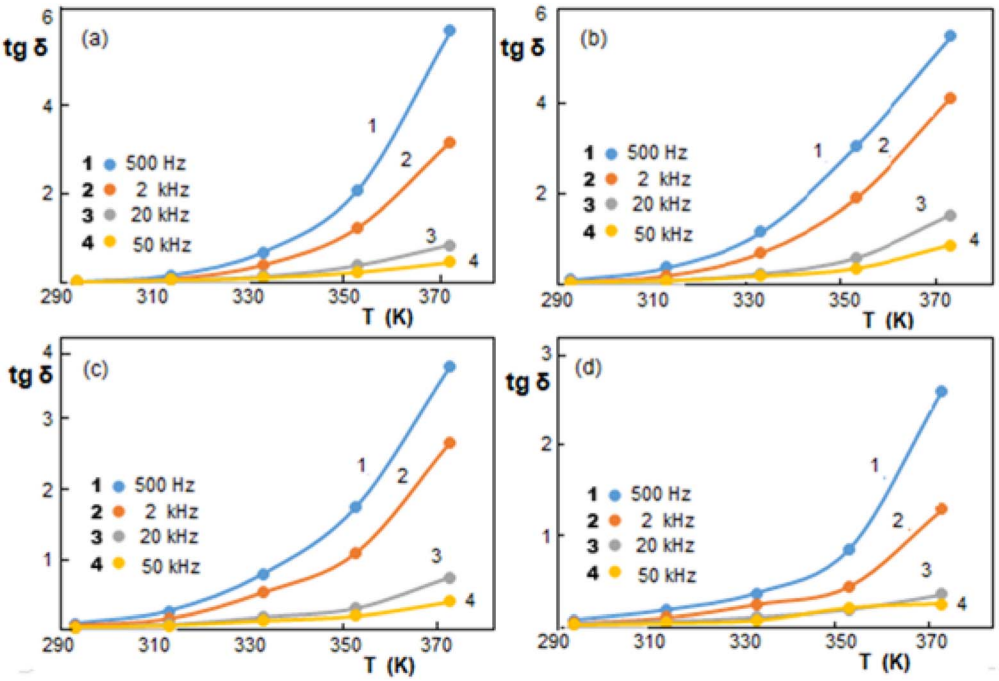


Fig. 10 The tg $\delta \sim T$ dependence for different frequency (500 Hz, 2 kHz, 20 kHz and 50 kHz) of (a) unirradiated-(N0), (b) 500 kGy-(N1), (c) 1500 kGy-(N2), (d) 2500 kGy-(N3).

The observed shift indicates a reduced relaxation time at this dose. In contrast, other samples show relaxation at lower frequencies, likely due to the presence of less mobile oxygen-containing groups formed at higher doses, which increase the relaxation time.

Let us now examine how the increase in dielectric loss tangent (tg $\delta$) behaves with respect to temperature at different frequencies. Fig. 10 illustrates the temperature dependence of tg $\delta$ at various frequencies (500 Hz, 2 kHz, 20 kHz, and 50 kHz).

As seen from the graph, the value of the dielectric loss tangent (tg $\delta$) increases with temperature, particularly at lower frequencies. The sharp increase in tg $\delta$ observed at lower frequencies under low radiation doses indicates that interfacial polarization is significantly enhanced by gamma irradiation. When the radiation dose reaches 1500 kGy, the polymer chain scission process becomes dominant. Nevertheless, the tg $\delta$ value at this dose remains higher than that of the unirradiated sample. This can be attributed to the fragmented polymer chains infiltrating the interlayer regions of the $FeGaInS_4$ crystal, thereby enhancing interfacial polarization.[53,54]

However, the decrease in tg $\delta$ at 1500 kGy compared to the 500 kGy sample is likely due to the transformation of oxygen-containing groups into relatively immobile functional groups, possibly through further binding with oxygen or hydrogen atoms. The reduced mobility of these groups lowers polarization and decreases energy dissipation during alignment with the electric field.

At higher doses, such as 2500 kGy, the tg $\delta$ value decreases even further. This behavior can be explained by the formation of radiation-induced defects around the filler particles, which suppress interfacial polarization. Notably, at this high dose, the irradiated sample exhibits higher tg $\delta$ values than the unirradiated one only at low frequencies, further confirming that gamma radiation adversely affects interfacial polarization at high doses.[53–56]

It is important to note that the frequency dependence of dielectric loss is closely related to the underlying conduction mechanism, which evolves with both temperature and radiation dose.

The frequency dependence of dielectric loss is dependent on the conduction mechanism.[37–40] It is known that in the hopping mechanism ($0.1 \leq s \leq 1.0$), dielectric loss behaves in a frequency-dependent manner. Based on the above, the frequency dependence of the dielectric loss angle tangent for different conduction mechanisms can be expressed as follows:

$$\text{tg}\,\delta(\omega) \sim (\omega^{-1} + \omega)\ \text{Zone Mechanism} \quad (15)$$

$$\text{tg}\,\delta(\omega) \sim \omega(\omega^{S-2} + 1)\ \text{Hopping Mechanism} \quad (16)$$

From eqn (15), it is evident that in conductivity, the zone mechanism plays a dominant role. The relationship of $\text{tg}\,\delta \cdot \omega = f(\omega)$ has been established, and the $\ln(\text{tg}\,\delta \cdot \omega)$ *versus* $\ln \omega$ graph has been plotted for different temperatures for the samples (a) unirradiated, (b) irradiated at 500 kGy, (c) irradiated at 1500 kGy, and (d) irradiated at 2500 kGy (Fig. 11).

As seen in the figure, although the obtained curves for the studied samples exhibit segments that are nearly linear, they

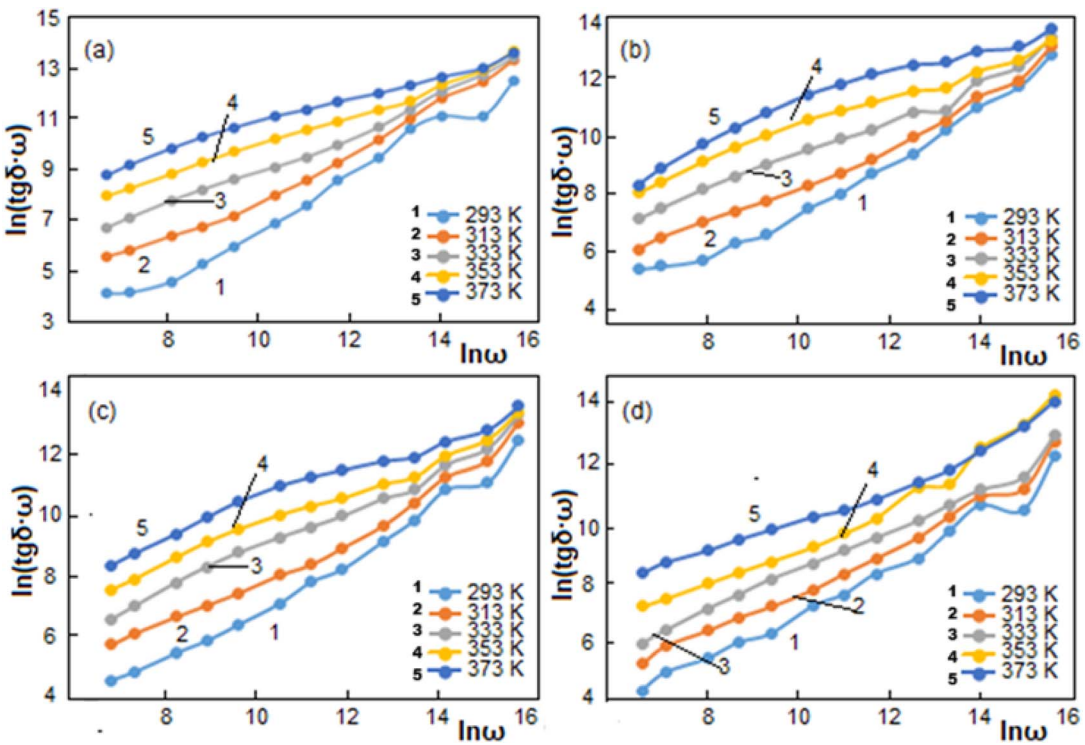


Fig. 11 The $\ln(\text{tg}\,\delta \cdot \omega) \sim \ln \omega$ dependence for different temperatures of (a) unirradiated-(N0), (b) 500 kGy-(N1), (c) 1500 kGy-(N2), (d) 2500 kGy-(N3).

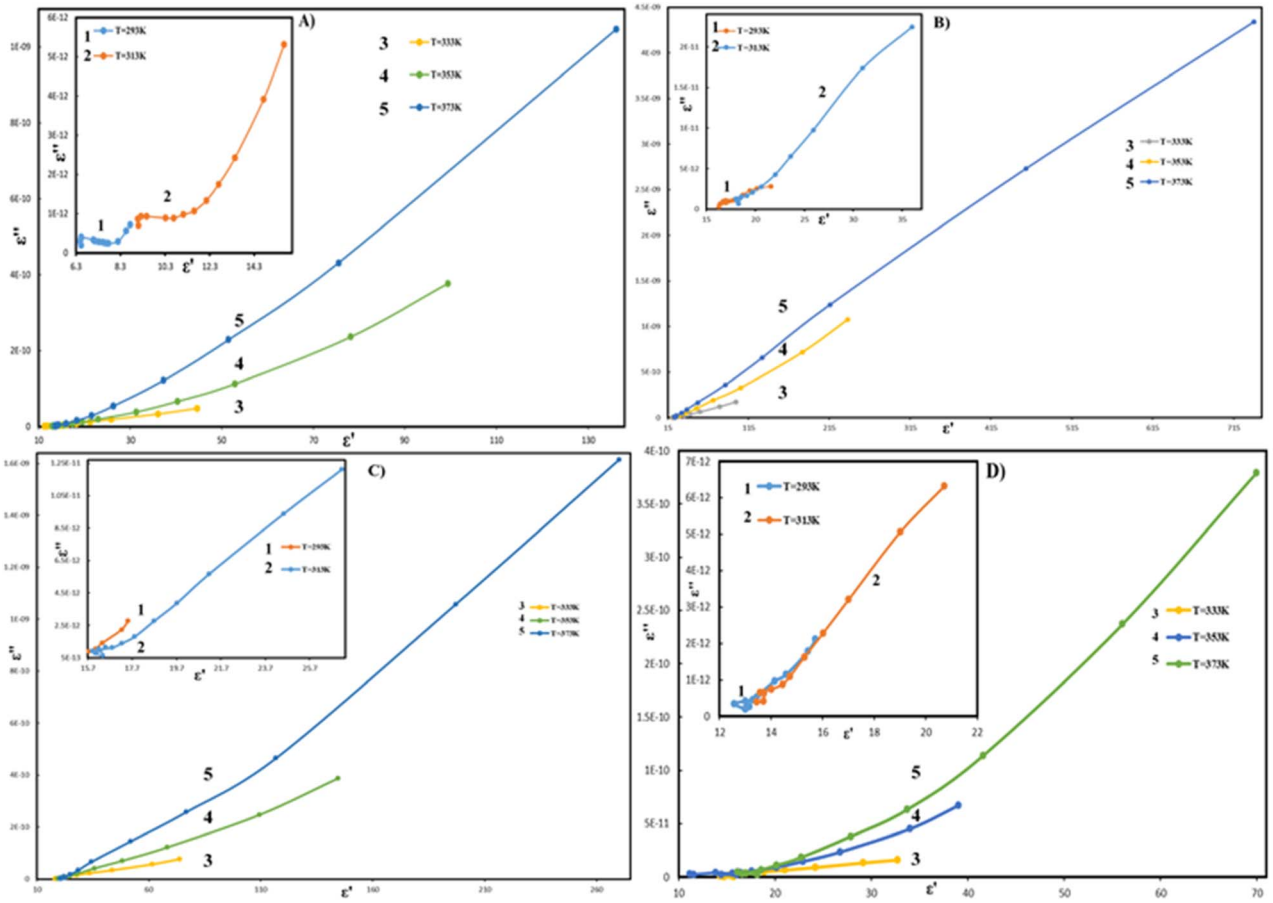


Fig. 12 The Cole–Cole plot of (a) unirradiated-(N0), (b) 500 kGy-(N1), (c) 1500 kGy-(N2), (d) 2500 kGy-(N3) at 293–373 K.

deviate from perfect straight-line behaviour. This observation suggests that for the composites (a) unirradiated, (b) irradiated at 500 kGy, (c) irradiated at 1500 kGy, and (d) irradiated at 2500 kGy, the conduction process is governed by a combination of zone conduction and hopping mechanisms.[37–39]

Therefore, the electrical conductivity in PVA+3 wt% $FeGaInS_4$ composites across all radiation doses is best described by a mixed zone-hopping conduction model, where both extended-state (band-like) and localized-state (hopping) charge transport contribute to the overall behaviour.[35]

Fig. 12 shows the Cole–Cole plots measured over the frequency range of 120 Hz–1 MHz at temperatures from 293 K to 373 K for (a) the unirradiated sample, (b) the sample irradiated at 500 kGy, (c) the sample irradiated at 1500 kGy, and (d) the sample irradiated at 2500 kGy.

The graph shows that in the non-irradiated sample, the relaxation deviates significantly from the Debye model. This can be attributed to the heterogeneity of the samples and the presence of a polymer–filler interphase, which results in a complex relaxation mechanism. When the samples are exposed to 500 kGy radiation, the lower region of the graph shows reduced disorder, and the overall curve begins to bend, resembling the Debye model. This behavior is explained by the onset of crosslinking due to radiation, which increases the structural order in the polymer-based composite.

At higher radiation doses, this bending decreases, and at 2500 kGy, a more pronounced linearity is observed. This effect is attributed to polymer chain degradation and scission at high doses, which alters the polymer–filler interactions and increases the contribution of components with different relaxation characteristics.

According to the correlated barrier hopping (CBH) model, the diameter of the Cole–Cole plots is strongly dependent on temperature. As the temperature increases, the hopping probability of charge carriers rises, the polymer matrix softens, and carrier mobility is enhanced. Consequently, both bulk and interfacial resistances decrease, while the values of the dielectric constants ($\varepsilon'$ and $\varepsilon''$) increase.[56,57]

As seen in the figures, with rising temperature, the radius of the Cole–Cole arcs significantly decreases, and their shapes change markedly. This temperature-dependent behavior of impedance, along with the non-Debye nature of relaxation, clearly indicates that the conduction in the composite occurs *via* the correlated barrier hopping (CBH) mechanism.

Therefore, the reduction in impedance and the pronounced shift of the Cole–Cole plots with increasing temperature confirm that the hopping process is thermally activated and validate the consistency of the electrical conduction mechanism in the samples with the CBH model.

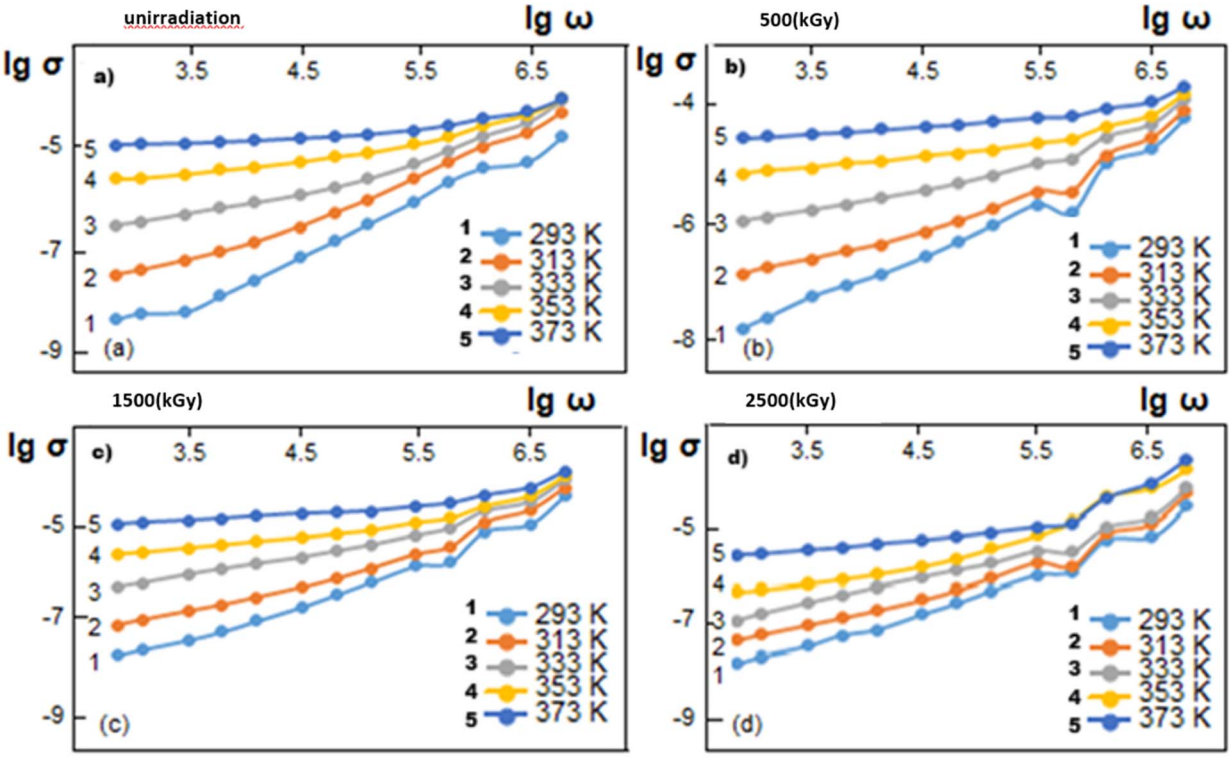


Fig. 13 Dependence of conductivity on the frequency of the electric field at temperatures ranging from 293 K to 373 K for the composites: (a) unirradiated-(N0), (b) 500 kGy-(N1), (c) 1500 kGy-(N2), (d) 2500 kGy-(N3).

Fig. 13 illustrates the frequency dependence of electrical conductivity for PVA+3 wt% $FeGaInS_4$ composites under varying temperatures and gamma radiation doses.

The graph clearly shows that electrical conductivity increases with increasing frequency, consistent with Joshers' universal power law ($\sigma_{ac}(\omega) = A\omega^S$). This behaviour suggests that the conduction mechanism is governed by the hopping of charge carriers between localized states, specifically *via* the correlated barrier hopping (CBH) model.[37–40]

Additionally, as the temperature increases from 293 to 373 °C, the electrical conductivity also increases. This can be attributed to the fact that higher temperatures activate localized charge centers and facilitate charge carrier transitions, thereby enhancing conductivity.[37–40]

From the graph, it is also evident that at room temperature, the sample exposed to 500 kGy of radiation exhibits the highest conductivity. However, with further increases in radiation dose, the conductivity decreases. Although radiation at room temperature does influence the conductivity, it does not reduce it below the value observed for the unirradiated sample. This implies that, under these conditions, radiation still contributes positively to charge transport.

The enhanced conductivity at 500 kGy can be explained by the formation of new bonds and crystalline domains, which bring localized charge centers closer together and create additional hopping sites. Furthermore, newly formed oxygen-containing functional groups may introduce trap states, which lower the energy barrier for hopping and facilitate CBH or Mott-type conduction.[38]

At 1500 kGy, polymer degradation becomes significant, increasing the distance between hopping centers, which in turn reduces conductivity.

In the case of 2500 kGy, a marked decline in conductivity is observed. This is likely due to the formation of deep-level defects (deep impurities) within the crystal structure. These defects act as charge traps, reducing the number of free carriers available for conduction. Thus, the observed reduction in conductivity with increasing radiation dose can be attributed to the emergence of such radiation-induced deep-level centers.[62,63]

Temperature also plays a crucial role in modulating the conductivity mechanism, particularly at higher radiation doses. For the 2500 kGy irradiated sample, increasing the temperature does not enhance conductivity beyond that of the unirradiated sample. While temperature can sometimes anneal defect states formed under low-dose radiation or from other causes, deep-level defects induced by high radiation doses require significantly higher temperatures for annealing.[64] Consequently, at 373 K, the conductivity of the unirradiated sample increases due to annealing of shallow defects, whereas in the 2500 kGy sample, the deep defects remain unaffected, resulting in lower conductivity.

From the $\lg \sigma(\omega)$ dependency, it is evident that as the frequency increases, the electrical conductivity increases. For the studied samples, in the frequency range of $1.2 \times 10^2$ to $10^6$ Hz, the relationship holds true.

$$\sigma \sim \omega^{S} \quad (17)$$

The dynamic changes in the exponent $s$ (eqn (17)) as a function of temperature are crucial for determining the type of conductivity in the material. In the case of quantum mechanical tunnelling (QMT), the exponent $s$ increases with increasing temperature. In the classical hopping mechanism through a potential barrier (HOB), $s$ is equal to 1. However, in the correlated barrier hopping (CBH) model, $s$ decreases as temperature increases.[65]

In polymer materials, two primary charge transport models are observed: quantum mechanical tunnelling (QMT) and correlated barrier hopping (CBH).

To determine the type of electrical conductivity mechanism in the studied materials—PVA/3 wt% $FeGaInS_4$ composites under different radiation doses such as (a) unirradiated, (b) 500 kGy, (c) 1500 kGy, and (d) 2500 kGy – the frequency exponent values ($s$) were calculated from the experimental conductivity–frequency curves presented in Fig. 14.

The temperature dependence of the exponent $s$ for all samples is presented in Fig. 11. At frequencies of $5 \times 10^3$ Hz and 1 MHz, the observed decrease in the $s$ parameter with increasing temperature is indicative of a hopping conduction mechanism. According to the correlated barrier hopping (CBH) model,[33–39] electrons hop over potential barriers between localized energy states.

For all samples, within the temperature range of 293 K to 373 K and frequency range of $1.2 \times 10^2$ to $10^6$ Hz, the exponent $s$ remains nearly constant, varying between 0.14 and 1.52. At lower temperatures, the value of $s$ exhibits a stronger dependence on frequency, whereas at higher temperatures, the changes in $s$ with frequency become less pronounced.

On the other hand, it is known that if the dependence of electrical conductivity on frequency in materials follows the $\lg \sigma(\omega) \sim \omega^S$, $0{,}01 \leq s \leq 1{,}0$, the presence of a hopping conduction mechanism is assumed.[52–54]

Based on the obtained experimental data and using eqn (8)–(14), the system parameters for PVA/3%$FeGaInS_4$ based composites irradiated at various doses (unirradiation, 500 kGy, 1500 kGy and 2500 kGy) were calculated at a temperature of 373 K and a frequency of $5 \times 10^3$ Hz. Furthermore, based on the obtained experimental data and using eqn (5)–(8), the system parameters for PVA/3%$FeGaInS_4$ based composites irradiated at various doses (unirradiation, 500 kGy, 1500 kGy and 2500 kGy) were calculated at various temperatures and a frequency of $5 \times 10^3$ Hz. The obtained values are presented in Table 3.

As seen from the table, when the samples were exposed to 500 kGy of radiation, $R$ increases sharply, while $N$ and $W_M$ decrease significantly. In polymer composites, when crosslinking occurs, the electron states in the polymer chains move closer and merge, leading to a reduction in the concentration of available trap states. This happens because radicals generated during crosslinking form bonds with side chains of neighbouring polymer chains, resulting in a denser and more ordered

Table 3 Dielectric parameters of polymer composites

| Sample | $s$ | $R_\omega$, m·$10^{-10}$ | $N$, $m^{-3} \times 10^{27}$ | $W_M$, eV |
|---|---|---|---|---|
| N0 | 0, 94 | 3, 39 | 41, 45 | 2, 52 |
| N1 | 0, 82 | 8, 03 | 4, 15 | 0, 84 |
| N2 | 0, 85 | 6, 56 | 6, 71 | 1, 01 |
| N3 | 0, 88 | 5, 19 | 12, 53 | 1, 26 |

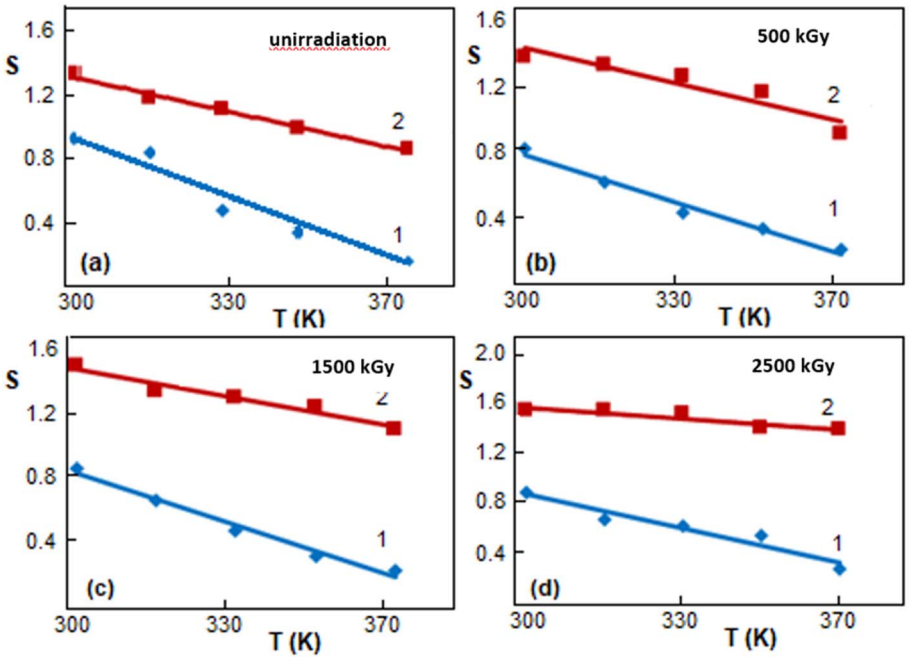


Fig. 14 Temperature dependence of the frequency exponent s for PVA+3 wt% $FeGaInS_4$ composites: (a) unirradiated-(N0), (b) 500 kGy-(N1), (c) 1500 kGy-(N2), (d) 2500 kGy-(N3). Frequencies: 1–5 × $10^3$ Hz, 2–1 × $10^6$ Hz.

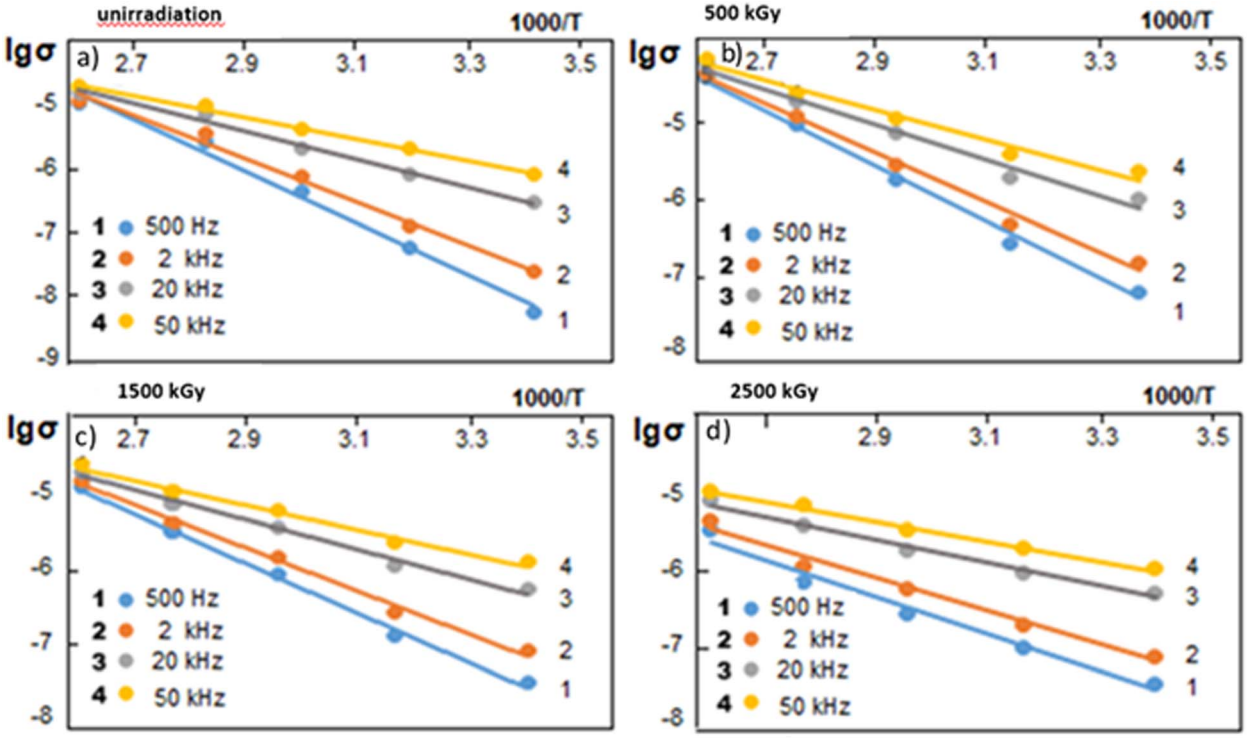


Fig. 15 Temperature dependence of electrical conductivity for composites: (a) unirradiated-(N0), (b) 500 kGy-(N1), (c) 1500 kGy-(N2), (d) 2500 kGy-(N3) at various electric field frequencies (500 Hz, 2 kHz, 20 kHz and 50 kHz).

polymer structure. Consequently, $N$ decreases sharply, and electrons need to jump further when they gain energy, which leads to an increase in $R$. Due to the increased structural ordering, the width of the potential wells for electrons decreases, and the depth of defects is reduced, which explains the significant decrease in $W_M$. At higher radiation doses, polymer chain scissions occur, creating new local electron states. This results in a decrease in $R$ and an increase in $N$ and $W_M$.

The temperature dependence of electrical conductivity for PVA and its composites at various electric field frequencies is presented. Fig. 15 illustrates how the electrical conductivity of PVA/3 wt% $FeGaInS_4$ composites, irradiated at different doses (nonradiated, 500 kGy, 1500 kGy, and 2500 kGy), varies with temperature across different frequencies of the applied electric field.

From the figure, it is evident that for both samples, within the studied frequency range ($2 \times 10^2$ to $5 \times 10^4$ Hz), the plot of $\log \sigma$ *versus* $10^3/T$ shows a linear behavior with different slopes. These slopes were used to determine the activation energies.

The experimentally calculated activation energies for the samples at different frequencies are presented in Table 4.

The activation energy values in the temperature range of 293 K to 353 K vary as follows: 0.81–0.34 eV for PVA+3wt% $FeGaInS_4$ (unirradiation), 0.74–0.4 eV for PVA+3wt.%$FeGaInS_4$ (500 kGy), 0.69–0.34 eV for PVA+3wt.%$FeGaInS_4$ (1500 kGy), and 0.5–0.27 eV for PVA+3wt.%$FeGaInS_4$ (2500 kGy). It can be observed that the activation energy of the nonirradiated PVA+3wt.% $FeGaInS_4$ composite differs only slightly from those of the composites irradiated with different gamma radiation doses. As seen from the table below, the activation energy decreases with increasing radiation dose.

This decrease in activation energy at lower doses is attributed to the formation of new crystallization centers-crosslinked structures and oxygen-containing groups—that act as local centres, reducing the hopping distance for electrons.[62–64] As the radiation dose increases, the traps and defects formed by radiation act as additional local centers for electrons. The increase in such local centers results in a lower energy requirement for hopping conduction.[60–68]

Since $FeGaInS_4$ is a layered semiconductor, the dispersion quality and the extent of the polymer–filler interface plays a decisive role in controlling the dielectric behavior of the composites. At low γ-irradiation doses (500 kGy), the induction of crosslinking within the PVA matrix increases its structural compactness and enhances the immobilization of the exfoliated $FeGaInS_4$ layers. This leads to a larger effective interfacial area and facilitates interfacial and dipolar polarization, which is reflected in the increase of $\varepsilon'$ and tan $\delta$. As the irradiation dose

Table 4 Activation energy of polymer composites

| Frequency | Unirradiation | 500 kGy | 1500 kGy | 2500 kGy |
|---|---|---|---|---|
| 500 Hz | 0, 81 eV | 0, 74 eV | 0, 69 eV | 0, 50 eV |
| 2 kHz | 0, 72 eV | 0, 66 eV | 0, 60 | 0, 43 eV |
| 20 kHz | 0, 42 eV | 0, 48 eV | 0, 48 eV | 0, 33 eV |
| 50 kHz | 0, 34 eV | 0, 40 eV | 0, 34 eV | 0, 27 eV |

increases (1500–2500 kGy), chain scission and defect formation become dominant, weakening the ability of PVA chains to interact with and anchor the $FeGaInS_4$ layers. The partial disruption of interfacial regions reduces charge accumulation and suppresses Maxwell–Wagner polarization, which is consistent with the observed decrease in dielectric constant and AC conductivity at high doses. Thus, the dose-dependent structural modifications of the PVA matrix directly govern the strength and effectiveness of interfacial coupling between $FeGaInS_4$ layers and the polymer environment.

# 4 Conclusion

In this study, the effect of γ-irradiation at various doses (500, 1500, and 2500 kGy) on 3 wt% $FeGaInS_4$/PVA composites—prepared by dispersing $FeGaInS_4$ semiconductor layered crystals within a PVA matrix—was comprehensively evaluated in terms of structural, optical, dielectric, and conduction properties. The selection of a wide irradiation dose window was motivated by the fact that γ-irradiation can induce two competing processes in PVA: crosslinking at low doses, which improves polymer stability, and chain scission at high doses, which leads to structural degradation. Understanding the balance between these processes is essential not only for fundamental interpretation but also for identifying the dose range suitable for potential applications of the composite.

XRD analysis revealed that low irradiation doses (particularly 500 kGy) promote effective crosslinking in the PVA matrix, resulting in enhanced structural ordering, increased crystallinity, and reduced crystallite size, while microstrain remained nearly unchanged. At higher doses, however, chain scission became dominant, leading to pronounced amorphization and lattice disorder.

UV-Vis spectroscopy showed that, irradiation treatment systematically decreases the absorbance of the composites. At low doses, cross-linking slightly reduces defect-related absorption. At 1500 kGy, the combined effects of chain scission and improved filler dispersion further lower absorption and scattering. At 2500 kGy, intensified chain scission and the elimination of intrinsic absorption centers lead to the minimum absorbance and maximum transparency. The Tauc analysis shows that $E_g$ of the polymer composites evolves non-linearly with radiation dose. At 500 kGy, cross-linking dominates, bringing trap states closer and resulting in a minimum $E_g$. At 1500 kGy, chain scission begins, defect sites move apart, and $E_g$ increases, though it remains slightly below the pristine value. At 2500 kGy, intense chain scission generates new deep defects, further widening $E_g$. Thus, the $E_g$ evolution is governed by the interplay between cross-linking and chain scission processes and the changing distribution of trap states. Low-dose irradiation (500–1500 kGy) reduces defects and stabilizes the structure, leading to a minimum Urbach energy ($E_u$). At the highest dose (2500 kGy), deep defects and structural degradation occur, causing a sharp increase in $E_u$.

Dielectric measurements demonstrated that low-dose crosslinking enhances dipolar polarization through the formation of additional functional groups and interfacial interactions, resulting in increased dielectric constant ($\varepsilon'$) and loss tangent ($\tan\delta$). Conversely, at 2500 kGy, defect-driven disorder suppressed polarization processes, leading to a noticeable decrease in these dielectric parameters.

The AC conductivity behaviour was well described by the CBH mechanism. At 500 kGy, newly created localized hopping centers facilitated charge transport, increasing conductivity. At 2500 kGy, the dominance of deep, non-conductive defects reduced the hopping probability. The observed decrease in activation energy with increasing dose further supports the enhanced hopping process induced by radiation-modified local environments.

Importantly, γ-irradiation–induced crosslinking is known to decrease the water solubility of PVA and improve its mechanical strength, elasticity, chemical resistance, and thermal stability—properties highly relevant for applications such as radiation-resistant coatings, dielectric components, flexible electronics, packaging films, and hydrogels. Therefore, identifying the optimal dose (500 kGy in this study) where crosslinking enhances structural and dielectric performance without triggering significant degradation is crucial for extending the functional applicability of $FeGaInS_4$/PVA composites.

# Author contributions

Zeynab Addayeva – investigation, data curation, writing – original draft, writing – review & editing, project administration. Mustafa Muradov – conceptualization, methodology, validation, supervision. goncha eyvazova – software, visualization. Namiq Niftiyev – software, data curation. yashar azizian-kalandaragh- resources. faiq mammedov – resources.

# Conflicts of interest

The authors declare no competing interests.

# Data availability

The datasets generated and/or analyzed during the current study are available from the corresponding author upon reasonable request.

# Acknowledgements

The authors express their sincere gratitude to the COST Action CA20126 Network for Research, Innovation, and Product Development on Porous Semiconductors and Oxides for its financial support of the experimental investigations conducted in this study. During the preparation of this work, the authors used ChatGPT (OpenAI) to improve English clarity. After using this tool, the authors reviewed and edited the content as needed and take full responsibility for the final content.

# References

1 R. Hsissou, R. Seghiri, Z. Benzekri, M. Hilali, M. Rafik and A. Elharfi, *Compos. Struct.*, 2021, **262**, 113640.

2 S. Ramakrishna, J. Mayer, E. Wintermantel and K. W. Leong, *Compos. Sci. Technol.*, 2001, **61**(9), 1189–1224.
3 K. Friedrich, S. Fakirov and Z. Zhang, *Polymer Composites: from Nano- to Macro-Scale*, Springer, 2005.
4 S. Lotfy, A. Atta and E. Abdeltwab, *J. Appl. Polym. Sci.*, 2018, **135**(15), 46146.
5 S. Nambiar and J. T. W. Yeow, *ACS Appl. Mater. Interfaces*, 2012, **4**(11), 5717–5726.
6 A. T. Naikwadi, B. K. Sharma, K. D. Bhatt and P. A. Mahanwar, *Front. Chem.*, 2022, **10**, 837111.
7 T. Zaharescu and M. Mariș, *J. Compos. Sci.*, 2022, **6**(4), 109.
8 S. Ahmad, R. Hammad and S. Rubab, *J. Electron. Mater.*, 2022, **51**(10), 5550–5567.
9 N. Touati, M. Kaci, H. Ahouari, S. Bruzaud and Y. Grohens, *Macromol. Mater. Eng.*, 2007, **292**(12), 1271–1279.
10 S. Idris, A. A. A. Bakar, C. T. Ratnam, N. H. Kamaruddin and S. Shaari, *Appl. Surf. Sci.*, 2017, **400**, 118–128.
11 M. C. Kane, R. J. Lascola and E. A. Clark, *Radiat. Phys. Chem.*, 2010, **79**(12), 1189–1195.
12 M. J. Martínez-Morlanes, P. Castell, V. Martínez-Nogués, M. T. Martinez, P. J. Alonso and J. A. Puértolas, *Compos. Sci. Technol.*, 2011, **71**(3), 282–288.
13 P. Castell, F. J. Medel, M. T. Martinez and J. A. Puértolas, *J. Nanosci. Nanotechnol.*, 2009, **9**(10), 6055–6063.
14 M. Muradov, E. Huseynov, M. Conradi, M. Malok, T. Sever and M. B. Baghirov, *RSC Adv.*, 2025, **15**(17), 13574–13582.
15 H. Mitsui, F. Hosoi and T. Kagiya, *Polym. J.*, 1973, **4**(1), 79–86.
16 A. Al Naim, N. Alnaim, S. S. Ibrahim and S. M. Metwally, *J. Radiat. Res. Appl. Sci.*, 2017, **10**(3), 165–171.
17 C. M. Kavitha, K. M. Eshwarappa, S. C. Gurumurthy, N. Karunakara and I. Mallikarjun, *Arab. J. Sci. Eng.*, 2024, **49**(7), 10137–10146.
18 V. R. Sunitha and S. Radhakrishnan, *Polym. Bull.*, 2020, **77**(2), 655–670.
19 M. R. Cleland, L. A. Parks and S. J. Cheng, *Nucl. Instrum. Methods Phys. Res., Sect. B*, 2003, **208**, 66–73.
20 F. M. Mammadov, I. R. Amiraslanov, M. A. Mahmudova and M. B. Babanly, in *Solid State Chemistry and Functional Materials-2018*. Thermodynamics and Materials Science, 2018, pp. 362.
21 F. M. Mammadov, D. M. Babanly, I. R. Amiraslanov, D. B. Tagiev and M. B. Babanly, *Russ. J. Inorg. Chem.*, 2021, **66**, 1533–1543.
22 N. N. Niftiev, A. O. Dashdemirov, F. M. Mamedov and M. B. Muradov, Surf. Eng, *Appl. Electrochem.*, 2023, **59**, 644–648.
23 F. M. Mammadov, N. Niftiyev and F. I. Mammadov, *Azerbaijan Chem. J.*, 2017, **2**, 56–59.
24 N. N. Niftiev, O. B. Tagiev, M. B. Muradov and M. F. Mamedov, *Semiconductors*, 2009, **43**(11), 1407–1409.
25 C. Gong and X. Zhang, *Science*, 2019, **363**, eaav4450.
26 S. Zhang, R. Xu, N. Luo and X. Zou, *Nanoscale*, 2021, **13**, 1398–1424.
27 M. Muradov, E. Huseynov, M. Conradi, M. Malok, T. Sever and M. B. Baghirov, *RSC Adv.*, 2025, **15**(17), 13574–13582.
28 M. B. Baghirov, M. Muradov, E. Huseynov, G. E. Kochari, R. F. Huseynali and M. Conradi, *Radiat. Phys. Chem.*, 2025, **226**, 112258.
29 M. Muradov, M. B. Baghirov, G. Eyvazova, L. Gahramanli, S. Mammadyarova, G. Aliyeva, *et al.*, *Radiat. Phys. Chem.*, 2023, **208**, 110926.
30 S. Mustapha, M. M. Ndamitso, A. S. Abdulkareem, J. O. Tijani, D. T. Shuaib, A. K. Mohammed and A. Sumaila, *Adv. Nat. Sci.: Nanosci. Nanotechnol.*, 2019, **10**(4), 045013.
31 M. Basak, M. L. Rahman, M. F. Ahmed, B. Biswas and N. Sharmin, *J. Alloys Compd.*, 2022, **895**, 162694.
32 G. G. Riungu, S. W. Mugo, J. M. Ngaruiya, G. M. John and N. Mugambi, *Am. J. Nanosciences*, 2021, **7**(1), 28–34.
33 P. R. Jubu, O. S. Obaseki, A. Nathan-Abutu, F. K. Yam, Y. Yusof and M. B. Ochang, *Results Opt.*, 2022, **9**, 100273.
34 P. H. Andrade, C. Volkringer, T. Loiseau, A. Tejeda, M. Hureau and A. Moissette, *Appl. Mater. Today*, 2024, **37**, 102094.
35 P. Makuła, M. Pacia and W. Macyk, *J. Phys. Chem. Lett.*, 2018, **9**(23), 6814–6817.
36 F. N. C. Anyaegbunam and C. Augustine, Dig, *J. Nanomater. Biostruct.*, 2018, **13**(3), 847–856.
37 Y. M. Poplavko, in *Electronic Materials*, Elsevier, 2019, pp. 287–408.
38 N. Mott, E. Davis, *Elektronnye Protsessy V Nekristallicheskikh Veshchestvakh*, Mir, Moscow, 1982, 662 pp.
39 S. R. Elliott, *Adv. Phys.*, 1987, **36**(2), 135–217.
40 A. A. Kononov, N. A. Nikonorova and R. A. Kastro, *FTP (Fizika i Tekhnika Poluprovodnikov)*, 2021, **63**(10), 1706–1710.
41 X. Hong, L. Zou, J. Zhao, C. Li and L. Cong, *IOP Conf. Ser.: Mater. Sci. Eng.*, 2018, **439**(4), 042011.
42 V. Kumar, Y. Ali, R. G. Sonkawade and A. S. Dhaliwal, *Nucl. Instrum. Methods Phys. Res., Sect. B*, 2012, **287**, 10–14.
43 A. El Rahman, H. S. Metwally, N. Sabry and M. I. Mohammed, *Sci. Rep.*, 2024, **14**(1), 27466.
44 E. A. Kamoun, O. I. Sallam, E. E. Khozemy, M. Morsy, Y. Al-Faiyz, S. M. Matar, *et al.*, *Mater. Adv.*, 2024, **5**(13), 5658–5670.
45 M. B. Baghirov, M. Muradov, G. Eyvazova, S. Mammadyarova, L. Gahramanli, G. Aliyeva, *et al.*, *RSC Adv.*, 2023, **13**(50), 35648–35658.
46 J. Bai, Y. He, J. Yang and W. Qi, *Sep. Purif. Technol.*, 2025, **364**, 132554.
47 S. M. Gafar, M. A. El-Kelany and S. R. El-Shawadfy, *J. Radiat. Res. Appl. Sci.*, 2018, **11**(3), 190–194.
48 A. M. Abdelghany, E. M. Abdelrazek, S. I. Badr and M. A. Morsi, *Mater. Des.*, 2016, **97**, 532–543.
49 E. A. Davis and N. F. Mott, *Philos. Mag.*, 1970, **22**(179), 903–922.
50 H. Elhosiny Ali, M. Abdel-Aziz, A. Mahmoud Ibrahiem, M. A. Sayed, H. S. M. Abd-Rabboh, N. S. Awwad, *et al.*, *Polymers*, 2022, **14**(9), 1741.
51 M. Muradov, M. B. Baghirov, G. Eyvazova, L. Gahramanli, S. Mammadyarova, G. Aliyeva, *et al.*, *Radiat. Phys. Chem.*, 2023, **208**, 110926.

52 M. Muradov, Z. Addayeva, N. Niftiyev, F. Mammadov, G. Eyvazova and M. B. Baghirov, *J. Mater. Sci.*, 2025, **60**(5), 2314–2327.
53 Z. Addayeva, M. Muradov, N. Niftiyev, F. Mammedov, G. Eyvazova and B. Coşkuner Filiz, *J. Mater. Sci.*, 2025, 1–16.
54 M. B. Baghirov, M. Muradov, Z. Addayeva, N. Niftiyev, F. Mammadov, G. Eyvazova and M. Conradi, *Mater. Technol.*, 2025, **59**(4), 647–653.
55 Z. Addayeva, Y. Azizian-Kalandaragh, N. Niftiyev, G. Eyvazova, F. Mammadov, M. Babanly, *et al.*, *J. Vinyl Addit. Technol.*, 2024, **30**(6), 1650–1658.
56 M. H. Makled, E. Sheha, T. S. Shanap and M. K. El-Mansy, *J. Adv. Res.*, 2013, **4**(6), 531–538.
57 K. S. Hemalatha, G. Sriprakash, M. V. N. Ambika Prasad, R. Damle and K. Rukmani, *J. Appl. Phys.*, 2015, **118**(15), 154103.
58 F. Ciuprina, T. Zaharescu and I. Pleşa, *Radiat. Phys. Chem.*, 2013, **84**, 145–150.
59 A. Anwar, D. Elfiky, A. M. Ramadan and G. M. Hassan, *Radiat. Phys. Chem.*, 2017, **134**, 14–18.
60 Y. Gao and B. X. Du, in *2012 International Conference on High Voltage Engineering and Application (ICHVEA)*, IEEE, 2012, pp. 229–232.
61 M. A. Khan, R. A. Khan, Haydaruzzaman, A. Hossain and A. H. Khan, *J. Reinf. Plast. Compos.*, 2009, **28**(13), 1651–1660.
62 S. M. Sze, Y. Li and K. K. Ng, *Physics of Semiconductor Devices*, John Wiley & Sons, 2021, p. 44.
63 S. M. Sze, *Semiconductor Physics and Technology (sizin verdiyiniz başlıq belədir)*, 1985.
64 G. F. Knoll, *Radiation Detection and Measurement*, John Wiley & Sons, 2010.
65 A. Gaines, D. Kodali, S. Jeelani and V. Rangari, *Coatings*, 2021, 119–138.
66 S. Barnoss, N. Aribou, A. J. Paleo, M. E. Achour and L. C. Costa, in *Proc. Eighth Int. Symp. Dielectric Materials and Applications (ISyDMA'8)*, 2024, pp. 245–256.
67 J. Victorin, A. Razpopov, T. Higo, R. Dziobek-Garrett, T. J. Kempa, S. Nakatsuji, *et al.*, *Sci. Rep.*, 2024, **14**(1), 28040.
68 S. N. Mustafaeva, M. M. Asadov and A. A. Ismaĭlov, *Phys. Solid State*, 2009, **51**(11), 2269–2273.